RSC Advances

PAPER

View Article Online
View Journal | View Issue

Cite this: *RSC Adv.*, 2021, **11**, 39646

Significantly enhanced photoresponse of carbon nanotube films modified with cesium tungsten bronze nanoclusters in the visible to short-wave infrared range

Hao Chen,[a] Junyi Zhu,[a] Yang Cao, *[a] Jinquan Wei, [b] Bocheng Lv,[c] Qianqian Hu[c] and Jia-lin Sun*[c]

Carbon nanotube (CNT) films are promising materials for application in ultra-broadband photodetectors because their absorption range covers the entire spectrum from ultraviolet to the terahertz region, and their detection mechanism is the bolometric effect. Because of the different and limited photothermal conversion efficiencies of CNTs with respect to various wavelengths, the response performance of existing photodetector devices is unsatisfactory, particularly in the infrared band. In this paper, we propose for the first time the use of cesium tungsten bronze (Cs_xWO_3) nanomaterials, which have strong infrared absorption and excellent photothermal conversion properties, to decorate a CNT film for construction of a Cs_xWO_3–CNT composite film photodetector. When compared with CNT-based film photodetectors, the proposed Cs_xWO_3–CNT composite film photodetector shows a significantly enhanced broadband photoresponse over the range from visible light (405 nm) to the short-wave infrared (1550 nm) region, with an average increase in responsivity of 400% and an average increase in specific detectivity of 549%. In addition, the Cs_xWO_3–CNT photodetector shows a fast photoresponse, with a rise time of only 28 ms, which represents a 30% improvement over that of the CNT photodetector. This paper thus provides a new concept for the design of a high-performance broadband photodetector.

Received 10th September 2021
Accepted 7th December 2021

DOI: 10.1039/d1ra06817b

rsc.li/rsc-advances

1. Introduction

Carbon nanotubes (CNTs) have excellent optical,[1,2] electrical,[3,4] thermal,[5–7] and mechanical[8–12] properties. In terms of their photoelectric conversion properties, CNTs represent a promising broadband photoelectric conversion material because of their ability to respond to ultra-wide spectrum light ranging from the ultraviolet (UV) to the terahertz region. Within this range, the photoresponse in the UV region is related to π-plasmon absorption, while the photoresponse in the visible light (VIS) to near-infrared (NIR) region is fundamentally linked to the interband transitions of the CNTs.[13–15] When it is extended to the mid-infrared and terahertz regions, the photoresponse is mainly caused by the plasmon resonance that occurs along the main axis of the CNTs.[16,17] The entire absorbed light spectrum over the UV to terahertz range can produce heating (with various conversion efficiencies) through electron–phonon interactions.

At present, depending on the dominant mechanism, CNT photodetectors can be divided into two main categories. One type of CNT photodetector is based on the photogenerated electron–hole pair separation mechanism, where the photoexcited electron–hole pairs exist in the form of excitons. Because of their one-dimensional structures, CNTs have a strong exciton binding energy, which limits the photogenerated free carrier yield.[18] Researchers have made considerable efforts to improve the electron–hole pair separation efficiency in CNTs, with combination of CNTs with other materials to construct various composite structures proving to be an effective method. For example, Wang's group obtained good photoelectric response performance in the VIS to NIR region using ultra-thin single-walled CNT (SWCNT) films that were compounded with graphene.[19] Arnold's group obtained a good UV-VIS-NIR response when using semiconductor CNT films compounded with C_{60}.[20] However, photodetectors based on the mechanism of photogenerated electron–hole pair separation have an unavoidable drawback, in that the spectral range of their photoresponse is

[a]*School of Instrumentation Science and Opto-electronics Engineering, Beijing Information Science &Technology University, Beijing 100192, People's Republic of China. E-mail: caoyang@bistu.edu.cn*

[b]*Key Lab for Advanced Materials Processing Technology of Education Ministry, School of Materials Science and Engineering, Tsinghua University, Beijing 100084, People's Republic of China*

[c]*Collaborative Innovation Center of Quantum Matter, State Key Laboratory of Low-Dimensional Quantum Physics, Department of Physics, Tsinghua University, Beijing 100084, People's Republic of China. E-mail: jlsun@tsinghua.edu.cn*

limited by the CNT energy gap, making it impossible to achieve broad-spectrum light detection. Therefore, CNT photodetectors based on this mechanism are mainly focused on detection of VIS and NIR signals.

Another CNT photodetector type is based on the thermal effects caused by the heat generation that occurs after light absorption, including photothermoelectric (PTE) devices and bolometric devices.[15,21–23] Among these devices, the bolometer device structure is mainly based on a suspended CNT film, which makes the heat more difficult to dissipate when compared with dissipation from CNTs on a substrate. The heat is mainly transferred through the contact area between adjacent CNTs, which causes a change in the resistance of the CNT-based device. The high thermal conductivity of CNTs forms the basis for the rapid response of this device type.[5,24] In 2018, Liu *et al.* reported an ultra-broadband bolometric photodetector based on suspended CNTs. The effect of the thermal resistance dominates the photoresponse during illumination over the range from UV to the terahertz region.[24] However, the device performance is still unsatisfactory, with further improvement required in the infrared (IR) band in particular, and few studies have reported on enhancement of the performance of CNT devices based on the bolometric effect to date.

In recent years, the excellent shielding ability of cesium tungsten bronze nanomaterials in NIR light have made them highly attractive for applications in the photothermal field. Tungsten bronzes are a series of nonstoichiometric compounds with the chemical formula M_xWO_3 ($0 < x < 1$), where x is an indeterminate value that can vary from 0 to 1 based on the number of interstitial cations, and M is usually an alkali metal, an ammonium ion, or a rare earth metal ion.[25,26] Cesium tungsten bronze (chemical formula: Cs_xWO_3) means that cesium ions (Cs^+) are used to dope the tungsten bronze structure. The special internal channel structure and carrier transfer characteristics of this material give it exceptional optical properties. Cs_xWO_3 nanomaterials have high transmittance in the VIS region. Additionally, because of their localized surface plasmon resonance[27] and small polariton jumps,[28] Cs_xWO_3 nanomaterials also exhibit strong IR absorption over a wide range from 800–2500 nm.[29–32] More importantly, these nanocrystals can instantly convert absorbed light energy into thermal energy with high conversion efficiency.[33] Therefore, Cs_xWO_3 is an excellent photothermal material.

This paper proposes for the first time that cesium tungsten bronze nanomaterials are used to modify the surfaces of CNT films, and the strong light absorption and high photothermal conversion efficiency of the cesium tungsten bronze nanomaterials are then used to improve the wide-spectrum detection performance of CNTs device significantly *via* their thermal effect mechanism. In this work, a suspended CNT thin film structure modified with Cs_xWO_3 nanoclusters (Cs_xWO_3–CNT) for a photodetector was fabricated by drop-casting of a Cs_xWO_3 nanosheet dispersion onto a suspended CNT film. The effect of the amount of cesium tungsten bronze used on the detector performance was studied systematically, and the optimal amount of cesium tungsten bronze was determined. When compared with the conventional CNT device, the performance of the Cs_xWO_3–CNT device shows significant improvement. Over the wide spectrum range from the VIS region to the short-wave infrared (SWIR) region (405–1550 nm), the average increase in specific detectivity was 549%, the average increase in responsivity was 400%, and the highest responsivity of 99.65 mA W^{-1} was achieved at 405 nm (VIS) under 0.625 W irradiation. In terms of response time, the Cs_xWO_3–CNT device exhibits a fast response time of 28 ms, which is 30% faster than the response of the CNT-based device. Cesium tungsten bronze nanocluster modified CNT film detectors are simple to manufacture and offer a new route toward the development of high-performance broadband photodetectors.

2. Experimental

2.1. Preparation and characterization of materials

The CNT films used in this paper were prepared by the floating catalytic chemical vapor deposition (CVD) method.[34] Each film has a network structure composed of a mixture of metallic CNTs and semiconducting CNTs and also has a variety of chiral properties,[24] thus meaning that the film has a variety of optical and electrical properties. The well-dispersed Cs_xWO_3 nanosheets used in this work were prepared by a water controlled-release process[32] and were formulated into an ethanol dispersion with a concentration of 0.78 mg mL^{-1}. The morphologies of both the suspended CNTs and the Cs_xWO_3–CNT composite films were characterized *via* field emission scanning electron microscopy (FESEM; Hitachi S-4800). The morphology, size, and crystal structure of the Cs_xWO_3 nanomaterials were characterized using transmission electron microscopy (TEM; JEM-2100F, JEOL, Japan). X-ray diffraction (XRD) patterns of the CNT film, the Cs_xWO_3 nanosheets and the Cs_xWO_3–CNT composite film were recorded on a X-ray diffractometer (XRD; Shimadzu XD-1). In order to characterize the thickness of the CNT film, the film is transferred onto a clean silicon wafer, and then ethanol is dropped onto the CNT film surface to make the CNT film closely adhere to the silicon wafer substrate. After the ethanol is dried, the film thickness is measured using an atomic force microscope (AFM; MultiMode 8, Bruker, USA). The absorption spectrum of the Cs_xWO_3 dispersions over the 400–2000 nm wavelength range was measured using a UV-VIS-NIR spectrophotometer (Cary 7000, Agilent, USA). The transmission spectra of the CNT film and the Cs_xWO_3–CNT composite film in the 400–2000 nm wavelength range were recorded using an integrating sphere attachment on the above spectrophotometer.

2.2. Fabrication of devices

First, a plexiglass substrate was prepared with a 10 mm-long and 5 mm-wide hollow at its center and it was then cleaned *via* an ultrasonic cleaning process. Two pieces of carbon conductive tape were cut to lengths of 5 mm and pasted on both ends of the hollow area of the plexiglass substrate. The side of the plexiglass substrate with the conductive adhesive tape was then pressed onto the graphite paper on which the CNT film was grown. Because of the adhesive nature of the conductive tape, a CNT film with the same width as the conductive tape was

adhered to the tape and suspended at both ends of the hollow area. In this way, the CNT film that was grown on graphite paper was transferred successfully to a skeletonized plexiglass substrate with a hollowed out center and the suspended CNT film was obtained. Then, a specified volume of the ethanol dispersion of Cs_xWO_3 was drop-cast onto the suspended CNT film surface to obtain the suspended Cs_xWO_3–CNT composite film. After natural drying of the dispersion, gold interdigital electrodes were deposited on the surface of the suspended CNT film and on the side of the Cs_xWO_3–CNT composite film without the Cs_xWO_3 by vacuum thermal evaporation using shadow masks, where these electrodes had a spacing of 200 μm and widths of 200 μm. Finally, the two terminals of the interdigitated electrodes were bonded with copper wires using silver paint to perform the subsequent electrical measurements. The effective working area of the device was 3 mm × 3 mm.

2.3. Photoelectric measurements

All tests were performed in a room temperature air environment. The current–voltage (*I–V*) characteristics and the dynamic optical responses of the CNT devices and the Cs_xWO_3–CNT devices were measured using a Keithley 2400 source meter. VIS irradiation was achieved using a 405 nm laser with a spot diameter of ~2.5 mm (MDL-III-405; 100 mW) and a 532 nm semiconductor laser with a spot diameter of ~1.2 mm (MGL-III-532; 200 mW). NIR irradiation was achieved using a 808 nm laser with a spot diameter of ~3.5 mm (MDL-III-808; 100 mW) and a 1064 nm laser with a spot diameter of ~1.5 mm (MIL-III-1064; 500 mW). SWIR irradiation was achieved using a 1550 nm laser with a spot diameter of ~1 mm (MDL-III-1550; 30 mW). All lasers mentioned above were purchased from Changchun New Industries Optoelectronics Technology. All light was incident from the side of the film without any electrodes. The laser spot position on the sample surface was controlled accurately by mounting the samples on a platform with two micrometer calipers that could be adjusted in both the horizontal and vertical directions. The optical power incident on the sample was adjusted using neutral density filters. The turn-on and turn-off operations for the illumination were performed using an electromagnetic shutter (SSH-C2B, OptoSigma). The surface temperature of the device operating area was monitored using an IR thermal imaging camera (DL700, Dali Technology).

3. Results and discussion

3.1. Morphology, structure and optical properties of materials

FESEM observations (Fig. 1a) showed that the CNTs are disorderly and are interleaved with each other to form a mesh-like structure. The inset in Fig. 1a shows that the CNT bundles have diameters of 10 to 30 nm and lengths of several micrometers or more,[34] indicating that these CNTs have a very large aspect ratio. TEM observations (Fig. 1b) showed that the as-prepared Cs_xWO_3 nanomaterials are formed in sheet-like structures. Fig. 1c shows the crystal structure of these Cs_xWO_3 nanosheets. The lattice spacing of 3.282 Å was identified as that

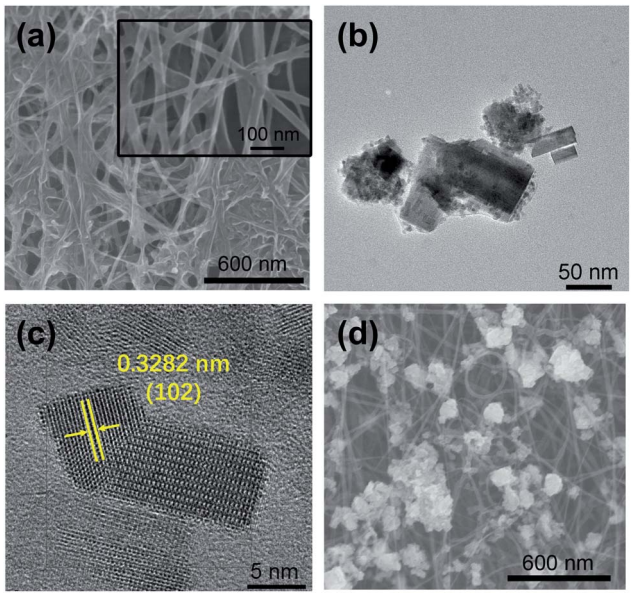

Fig. 1 (a) FESEM image of CNT films with low resolution, with a high resolution image shown in the inset. TEM images of Cs_xWO_3 nanosheets with (b) low resolution and (c) high resolution. (d) FESEM image of the Cs_xWO_3–CNT composite film.

of the (102) crystal plane. The FESEM images (Fig. 1d) show that the reticular structure of the CNT film remained unchanged after drop-casting of the Cs_xWO_3 nanosheet ethanol dispersion. The Cs_xWO_3 nanosheets aggregated into clusters with sizes ranging from 100 nm up to several hundred nanometers; these clusters were dispersed uniformly within the CNT network, thus forming a well-distributed Cs_xWO_3–CNT composite film system.

The crystal structure of the CNT film, the Cs_xWO_3 nanosheets and the Cs_xWO_3–CNT composite film were further characterized by XRD diffraction analysis. As shown in Fig. 2, black curve shows the XRD pattern of the Cs_xWO_3 nanosheets. All peaks could be indexed to the hexagonal cesium tungsten bronze (JCPDS no. 831334), which indicates that *x* value of is 0.32 in the Cs_xWO_3 molecular formula. Blue curve shows the

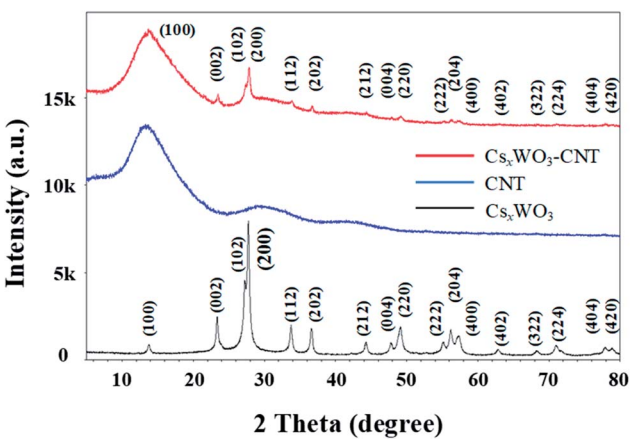

Fig. 2 XRD patterns of CNT film, Cs_xWO_3 nanosheets and Cs_xWO_3–CNT composite film (reference: $Cs_{0.32}WO_3$, JCPDS no. 831334).

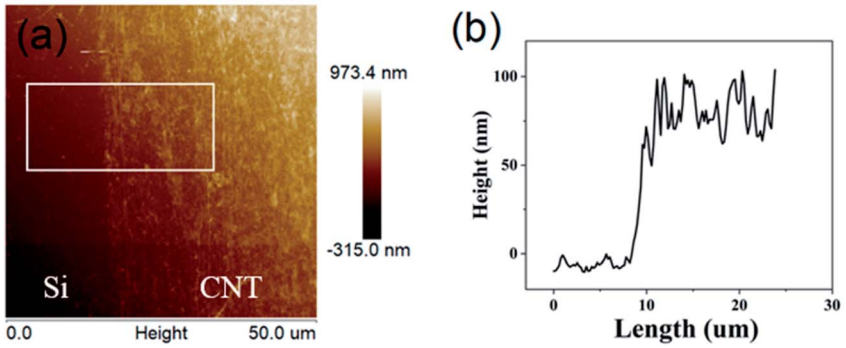

Fig. 3 (a) The AFM image of CNT film on silicon wafer substrate (b) The height profile corresponds to the white rectangular box region in (a).

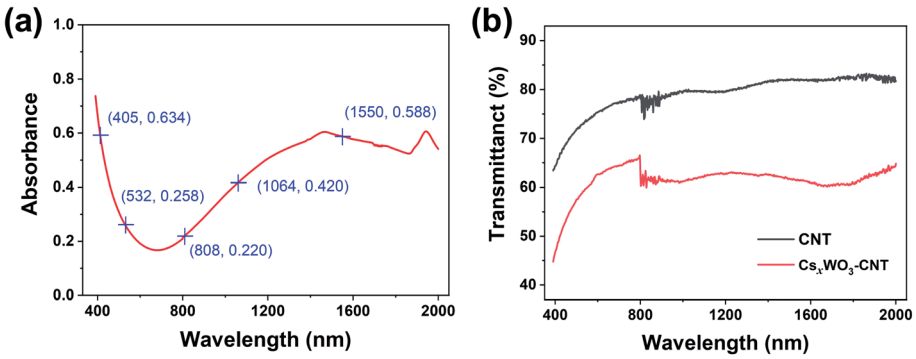

Fig. 4 (a) Absorbance spectrum of Cs_xWO_3 nanosheet dispersion. (b) Transmittance spectra of a suspended CNT film and a Cs_xWO_3–CNT composite film.

XRD pattern of the CNT film. The broad diffraction peaks were observed at 2θ of 14.1°, 29.5° and 43.4°. Red curve shows the XRD pattern of the Cs_xWO_3–CNT composite film. It is composed of the broad diffraction peaks of CNT and the sharp diffraction peaks of Cs_xWO_3, which indicates that Cs_xWO_3 and CNT in the Cs_xWO_3–CNT composite film remain the individual phase and crystallite properties.

The results of AFM measurements of the CNT film are shown in Fig. 3. Fig. 3a shows that the silicon substrate region and the CNT film region can be clearly distinguished. Fig. 3b shows the silicon wafer region is flat, while the height of the CNT film region is obviously fluctuating due to the network structure of the CNT film. The average thickness of the CNT film is 88.5 nm.

In addition, the optical properties of the Cs_xWO_3 nanosheet ethanol dispersion, the CNT film, and the Cs_xWO_3–CNT composite film were characterized. Fig. 4a shows the absorption spectrum of the dispersion of the Cs_xWO_3 nanosheets, which indicates that Cs_xWO_3 has strong light absorption in the IR band from 800–2000 nm, with an average absorbance of 46%. Because both the CNT film and the Cs_xWO_3–CNT composite film are reticular and thin (and almost semitransparent), the two films hardly reflect any light. Therefore, the absorbances of these films can be calculated using the following equation:

$$A = 100\% - T \quad (1)$$

where A and T are the absorbance and transmittance of the film, respectively. Fig. 4b shows the transmittance spectra of the suspended CNT film and the Cs_xWO_3–CNT composite film. The lack of smoothness in the two curves at around 800 nm is due to a change in the light source for the UV-Vis-NIR spectrophotometer. The results in Fig. 4b and eqn (1) thus allow the absorbances of the two films to be calculated. The results obtained indicate that when compared with the CNT film, the average absorbance of the Cs_xWO_3–CNT composite film is increased by 17.7% within the wavelength range from 400–2000 nm. In particular, the absorbance shows significant improvement in the IR band at wavelengths greater than 800 nm, where it is 19.2% higher than that of the CNT film.

3.2. Photoresponses of the devices

As shown in Fig. 5, a fully suspended CNT thin film device (Fig. 5a) and a Cs_xWO_3–CNT composite thin film device (Fig. 5b) were prepared based on a suspended CNT film and a CNT film modified with Cs_xWO_3 nanoclusters, respectively, which will be referred to as the CNT device and the Cs_xWO_3–CNT device, and the insets show the cross-sectional structures of the two films.

To obtain the best possible performance from the Cs_xWO_3–CNT device, the effect of the amount of Cs_xWO_3 present on the photocurrent of the Cs_xWO_3–CNT device was studied systematically. The light current (I_{light}) and the dark current (I_{dark}) are defined as the steady-state currents of the device under

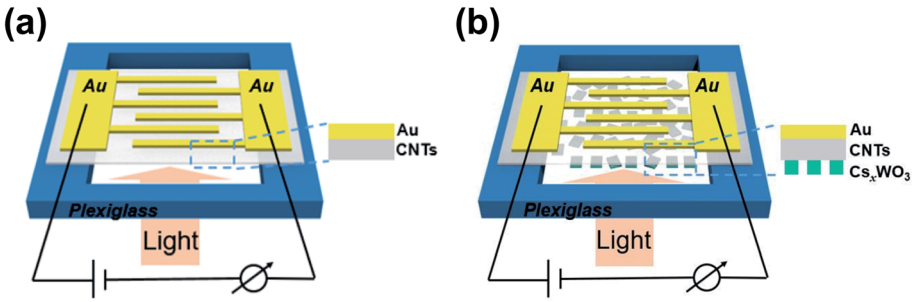

Fig. 5 Diagrams of (a) suspended CNT device and (b) suspended Cs_xWO_3–CNT device. The local cross-sections of the thin films are also shown.

illumination and in the dark, respectively. The photocurrent (I_{ph}) is defined as the difference between $|I_{light}|$ and $|I_{dark}|$, *i.e.*, $I_{ph} = |I_{light}| - |I_{dark}|$. The Cs_xWO_3 nanosheet ethanol dispersion with a concentration 0.78 mg mL^{-1} was drop-cast onto the CNTs film, with a volume of 5 μL being applied each time, and was allowed to dry naturally for 10 min before the I_{ph} of the device was tested. The drop-casting process above was repeated 16 times to increase the amount of Cs_xWO_3 on the CNT film surface from 0 μL to 80 μL. The I_{ph} values of the Cs_xWO_3–CNT device for each different amount of Cs_xWO_3 were measured separately, and the relationship between the Cs_xWO_3 dosage and the I_{ph} of the device was finally obtained; the results are shown in Fig. 6. When the amount of Cs_xWO_3 is in the 30–40 μL range, the I_{ph} of the device reaches its highest value, and as the amount of Cs_xWO_3 added continues to increase, the I_{ph} of the device then starts to decrease. This may be because the continued increase in the amount of Cs_xWO_3 causes the agglomeration of the Cs_xWO_3 nanosheets to become more severe, thus resulting in a continued increase in the size of the formed Cs_xWO_3 clusters. This would mean that the heat generated by light absorption in each Cs_xWO_3 cluster can only be transferred within the cluster itself and the heat cannot be conducted *via* contact to the CNTs, which then leads to the reduced device I_{ph}. Therefore, for the later study, the optimal volume of 35 μL of the Cs_xWO_3 nanosheet dispersion was used to modify the CNT film.

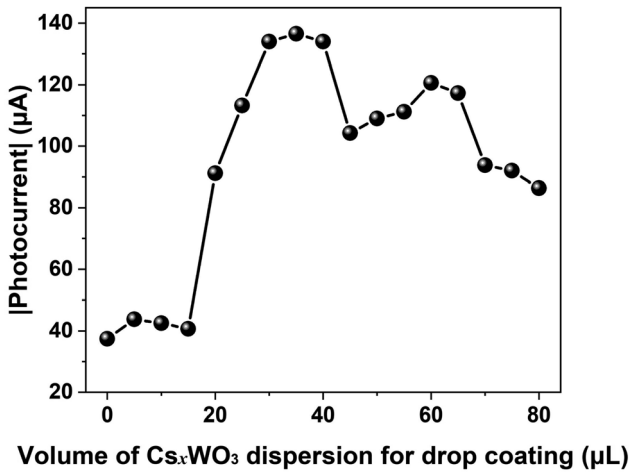

Fig. 6 Photocurrent as a function of the volume of the Cs_xWO_3 dispersion drop-coated on the CNT film surface under laser illumination at 532 nm of 2 mW under a bias voltage of −0.5 V.

The *I*–*V* characteristics of the CNT device and the Cs_xWO_3–CNT device in the dark and under light illumination are shown in Fig. 7. Regardless of the size of the positive bias voltage interval or the negative bias voltage interval within the bias voltage range from −0.8 V to +0.8 V, the absolute value of I_{light} is always lower than the absolute value of I_{dark}, which shows that the device resistance under illumination is greater than that in the dark, *i.e.*, the illumination causes an increase in the device resistance. The *I*–*V* characteristics of the two devices are linearly fitted over a bias voltage range of −0.1 V to +0.1 V, and the linearly fitted straight lines were extended to the entire bias voltage range, as shown by the dotted line in Fig. 7. It can be seen that the *I*–*V* characteristics are not strictly linear, but have weak nonlinearity, indicating that the CNT film is composed of metallic CNTs and semiconducting CNTs, and the metallic CNTs is dominant.

The photoresponses of the CNT device and the Cs_xWO_3–CNT device under on-off light modulation at various wavelengths are shown in Fig. 8. When the laser irradiates the devices, the photocurrent begins to increase rapidly in the negative direction until it reaches a stable value. When the laser is turned off, the photocurrent then decreases rapidly and returns to 0 mA. The most striking result here is that the photocurrents of the Cs_xWO_3–CNT devices are much higher than those of the CNT devices over the wide spectral range from the VIS to SWIR (405–1550 nm) regions under the same measurement conditions. These results show that the combination of the Cs_xWO_3 nanoclusters and the CNTs can enhance the photoresponses of the resulting devices significantly. Furthermore, the photoresponse mechanism can be understood from the data shown in Fig. 8. Regardless of the wavelength of the incident light (*i.e.*, of the energy of the photon), both devices show a negative photocurrent. This phenomenon again confirms that the absolute value of I_{light} is smaller than the absolute value of I_{dark}, which is consistent with the results of measurement of the *I*–*V* characteristics. This reveals that the dominant mechanism in the photoresponse is the increase in device resistance caused by heat generation after absorption of the photon energy, *i.e.*, the bolometric effect.

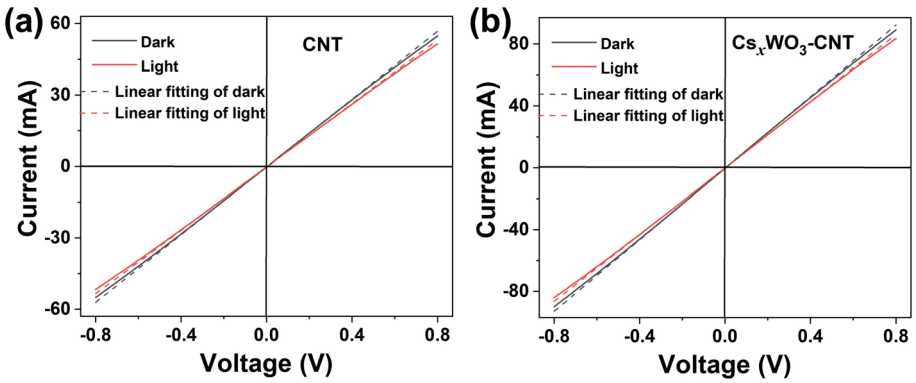

Fig. 7 The solid lines are the I–V characteristics of (a) CNT device and (b) Cs_xWO_3–CNT device under dark conditions and under VIS irradiation at 532 nm (7.5 mW). The dotted lines are extensions of the linear fitting in the range of −0.1 V to 0.1 V.

The responsivity (R_λ) is an important parameter for photodetectors and is defined as the photocurrent generated per unit power of the incident light. The responsivities of the CNT device and the Cs_xWO_3–CNT device under illumination at various wavelengths were calculated and the results are shown in Table 1. These results show that the responsivity of the Cs_xWO_3–CNT device is several times higher than that of the CNT device, and the average increase in responsivity was 400% over a wide spectral range from the VIS to the SWIR region (405–1550 nm). For the Cs_xWO_3–CNT device, the highest responsivity of 99.65 mA W^{-1} was achieved under irradiation with a power of 0.625 W at 405 nm (VIS) (see Fig. 9). The dominant mechanism in the photoresponse for both the Cs_xWO_3–CNT device and the CNT device is the bolometric effect. For the CNT device, the heat only comes from the light-to-heat conversion that occurs after the CNT film absorbs the light, while for the Cs_xWO_3–CNT device, the heat comes from the light-to-heat conversion process that occurs after the Cs_xWO_3 and the CNT film both absorb light. Of these materials, the Cs_xWO_3 nanocrystals can convert the absorbed photo-energy into local heat instantaneously with high conversion efficiency,[33,34] and the photothermal conversion efficiency of these nanocrystals is significantly higher than that of the CNT film (see Fig. 11 below and the related discussion). Therefore, the performance of the Cs_xWO_3–CNT device is a significant improvement over that of the CNT device.

An in-depth evaluation and analysis of the spectral performance of the Cs_xWO_3–CNT device is very important for application of the device. However, the laser spot area is different at each wavelength and the spot area for most wavelengths is smaller than the effective working area of the device. Therefore, to compare the performances of the Cs_xWO_3–CNT device at various wavelengths quantitatively, we also calculated the responsivity per unit spot area for each irradiation wavelength; this quantity is defined as $R'_\lambda = R_\lambda/S$, where R_λ and S are the responsivity and the spot area of the laser, respectively. All these results are summarized in Table 1.

The highest R'_λ value of the Cs_xWO_3–CNT device occurs at a wavelength of 532 nm. This is because the CNTs can provide their greatest thermal contribution to the Cs_xWO_3–CNT device at this wavelength. In the CNTs, the electrons that are excited by irradiation at 532 nm will all be de-excited in a nonradiative manner, while the de-excitation process in the other bands occurs in both photoemissive and nonradiative ways,[35] indicating that the CNTs have their highest thermal conversion efficiency at 532 nm. In addition, the second highest and third highest R'_λ values appear at wavelengths of 1550 and 1064 nm, respectively. This is mainly because of the high absorbance (see Fig. 2a) and the excellent photothermal conversion efficiency of the Cs_xWO_3 nanomaterials in the IR band. Furthermore, in the IR band (at 808, 1064, and 1550 nm), R'_λ continues to increase as the wavelength increases, which is mainly related to the higher absorbance property of Cs_xWO_3 at longer wavelengths, as Fig. 2a illustrates.

A Source Meter unit Keithley 2400 was used to obtain I_{dark} signal as a function of time. The bias voltage is −0.5 V same as the value applied when detecting the I_{light}. The recorded I_{dark} data was then converted to noise power spectral density using Fourier transformation. The square root of the noise power spectral density is the noise current spectral density. The total noise of the CNT device and the Cs_xWO_3–CNT device are 2.12×10^{-6} A $Hz^{-1/2}$ and 1.60×10^{-6} A $Hz^{-1/2}$ at a bandwidth of 1 Hz, respectively. This total noise value includes thermal noise, shot noise, and $1/f$ noise. Among them, the shot noise I_{nd} can be calculated according to the following formula.

$$I_{nd} = \sqrt{2eI_{dark}\Delta f} \quad (2)$$

where e and Δf denote the electron charge and the operating bandwidth of the detector, respectively, and I_{dark} is the dark current of the detector. The shot noise of the CNT device and the Cs_xWO_3–CNT device are 3.48×10^{-10} A $Hz^{-1/2}$ and 5.14×10^{-10} A $Hz^{-1/2}$, respectively. The thermal noise I_{nJ} of the two devices was also calculated according to the following formula.

$$I_{nJ} = \sqrt{\frac{4kT\Delta f}{R}} \quad (3)$$

where k, T and Δf are Boltzmann constant, thermodynamic temperature and the operating bandwidth of the detector, respectively, and the R is the resistance of the device in the dark. The thermal noise of the CNT device and the Cs_xWO_3–CNT device are 3.58×10^{-11} A $Hz^{-1/2}$ and 5.29×10^{-11} A $Hz^{-1/2}$,

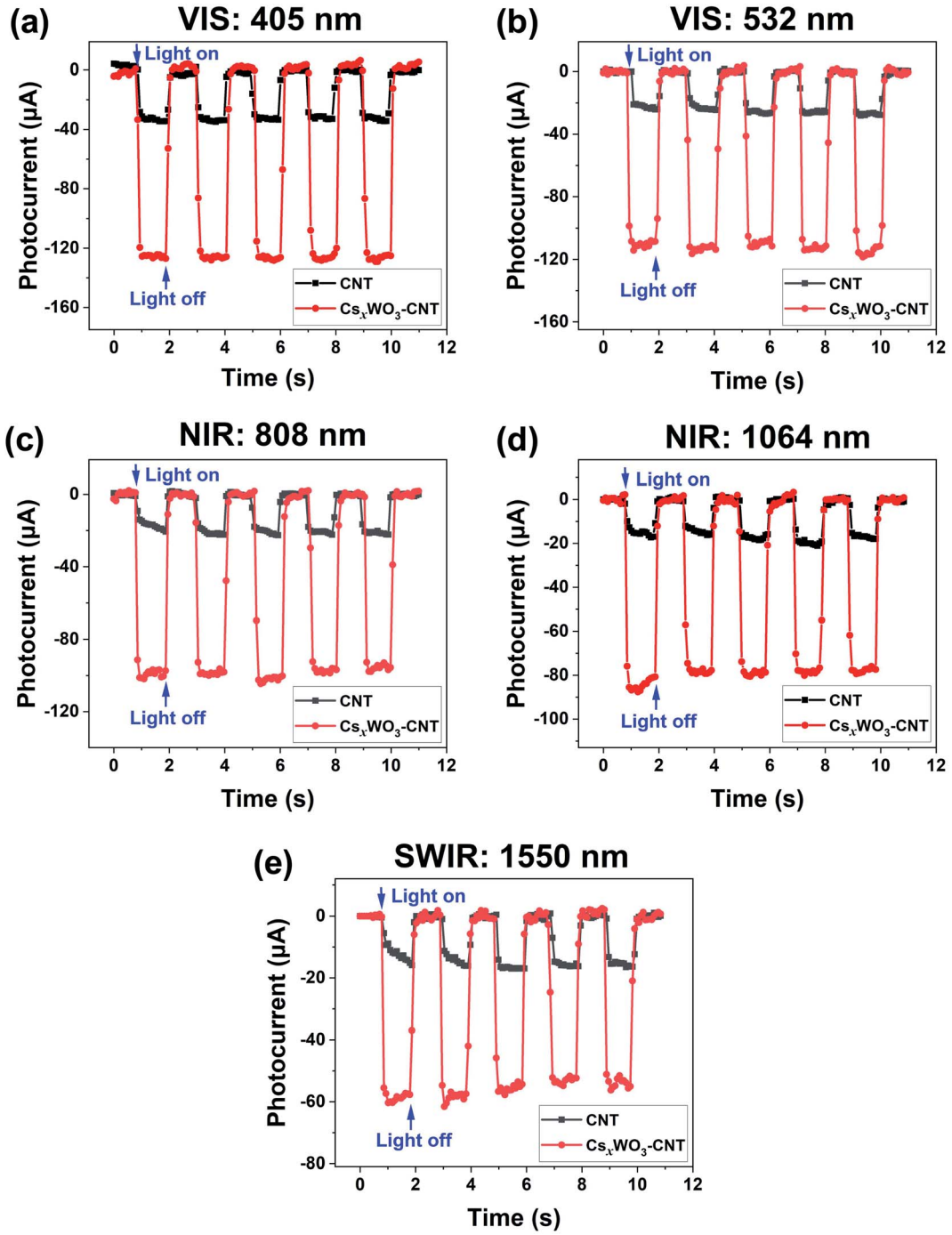

Fig. 8 Photoresponses of the CNT device and the Cs_xWO_3–CNT device under a bias voltage of −0.5 V. The incident laser wavelengths are (a) 405 nm (VIS), (b) 532 nm (VIS), (c) 808 nm (NIR), (d) 1064 nm (NIR), and (e) 1550 nm (SWIR), where all incident beams have an optical power of approximately 1.4 mW.

respectively. So $1/f$ noise of the CNT device and the Cs_xWO_3–CNT device are worked out as 2.1196×10^{-6} A $Hz^{-1/2}$ and 1.5994×10^{-6} A $Hz^{-1/2}$ which dominates the total noise. Based on the measured noise current spectral density, the specific detectivity (D^*) of the devices can be calculated according to the following formula.[36]

$$D^* = R_\lambda \frac{\sqrt{A}}{I_n} \quad (4)$$

where A, I_n and R_λ are the device area, the noise current spectral density and current responsivity, respectively. The specific detectivity values of the devices for different wavelengths are summarized in Table 1. Over the wide spectral range from the VIS to the SWIR band, the average increase in D^* is 549%, and

Table 1 Comparison of CNT device and Cs_xWO_3–CNT device under various wavelengths of light illumination in room temperature environment, where all incident beams have an optical power of approximately 1.4 mW

	CNT device				Cs_xWO_3–CNT device			
Wavelength (nm)	R_λ (mA W^{-1})	R'_λ (mA W^{-1} mm^{-2})	NEP (10^{-6} W $Hz^{-1/2}$)	D^* (10^6 Jones)	R_λ (mA W^{-1})	R'_λ (mA W^{-1} mm^{-2})	NEP (10^{-6} W $Hz^{-1/2}$)	D^* (10^6 Jones)
405	22.10	7.48	96.12	3.12	90.14	30.52	17.71	16.9
532	18.20	16.10	116.72	2.57	78.10	69.09	20.44	14.7
808	15.34	1.60	138.48	2.17	70.20	7.30	22.74	13.2
1064	13.25	7.50	160.33	1.87	56.30	31.88	28.36	10.6
1550	11.54	14.70	184.09	1.63	39.50	50.32	40.42	7.4

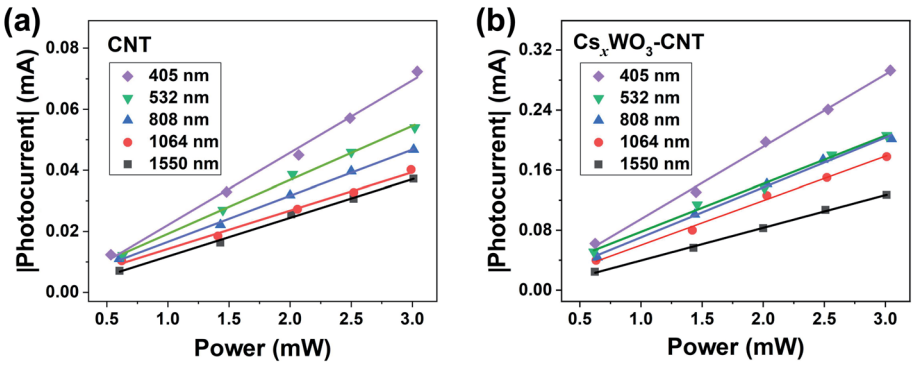

Fig. 9 Absolute value of photocurrent *versus* incident optical power for (a) CNT device and (b) Cs_xWO_3–CNT device. The optical power is approximately 1.4 mW at wavelengths of 405 nm (VIS), 532 nm (VIS), 808 nm (NIR), 1064 nm (NIR), and 1550 nm (SWIR), all under a bias voltage of −0.5 V.

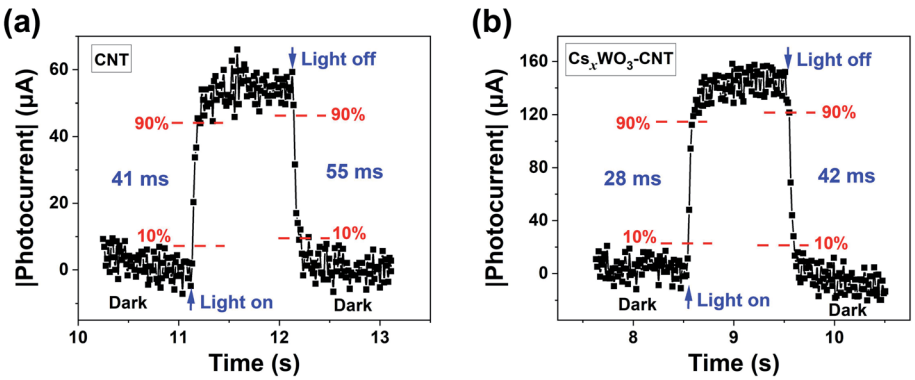

Fig. 10 Enlarged plots of individual on/off characteristics of (a) CNT device and (b) Cs_xWO_3–CNT device photoresponses under 532 nm irradiation with optical power of 3 mW at a bias voltage of −0.5 V.

the highest such increase is 609% at wavelength of 808 nm. Obviously, this increase in D^* is significantly higher than the corresponding increase in R_λ, because the device noise can be suppressed after modification of the Cs_xWO_3. The noise equivalent power (NEP) represents the lowest optical power that the detector can detect, and it can be calculated according to the following formula:

$$\mathrm{NEP} = \frac{I_n}{R_\lambda} \quad (5)$$

where I_n is the noise current of the detector, and R_λ is the current responsivity of the detector. The NEP value of each wavelength is shown in Table 1.

Fig. 9 shows that the photocurrents of both the CNT device and the Cs_xWO_3–CNT device are strongly proportional to the incident laser power within the range from 530 μW to 3 mW. The linear power detection range extends from microwatt to milliwatt levels, and can even be extended further to higher powers. This shows that the device is suitable for quantitative light detection applications.

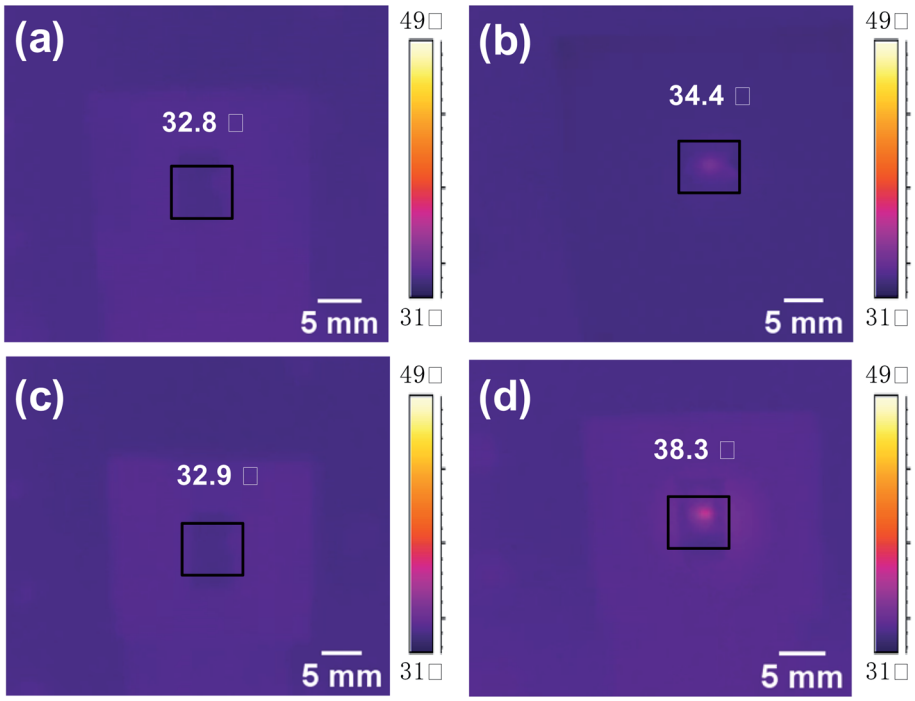

Fig. 11 Thermal images of (a and b) the CNT device and (c and d) the Cs_xWO_3–CNT device acquired by infrared thermography under identical conditions, where (a) and (c) were in the dark state and (b) and (d) were under illumination at 1064 nm (NIR) with optical power of 25.20 mW.

The response speed is also an important parameter for photodetectors. The rise time and the decay time of the photodetector represent the time gaps between 10% and 90% of the photocurrent peak values at the rising and falling edges, respectively. We calculated the response times of the two devices to irradiation of 3 mW at 532 nm. As shown in Fig. 10, the rise/fall times of the CNT photodetector are 41 ms/55 ms, and the rise/fall times of the Cs_xWO_3–CNT photodetector are 28 ms/42 ms. When compared with the CNT devices, the response time of the Cs_xWO_3–CNT photodetector is reduced significantly by 13 ms, and the response speed is improved by 30%. These fast device responses can be attributed to the ultra-high thermal conductivity of the CNTs, which also ensures that the CNTs can achieve rapid warming and cooling.[5] Corresponding to this high thermal conductivity, the CNTs also have a low specific heat capacity,[37] which allows the CNTs to change the film temperature rapidly when heated, meaning that all our devices show fast responses. In addition, the response speed of the Cs_xWO_3–CNT device is better than that of the CNT device. This higher response speed may be due to the Cs_xWO_3 nanocrystals having better dynamic characteristics during the heating and cooling processes than the CNTs.

The surface temperatures of the CNT device and the Cs_xWO_3–CNT device in the working area under the light and dark state conditions were captured using an infrared thermal imaging camera, and the results are shown in Fig. 11. Under 1064 nm NIR light illumination, both devices showed a temperature increase. For the CNT device, the temperature in

Table 2 Comparison of the Cs_xWO_3–CNT photodetectors and other representative reported CNT photodetectors based on the mechanism of bolometric effect

Material	Wavelength (μm)	Highest responsivity	Response time	Highest D^* (cm $Hz^{1/2}$ W^{-1})	Ref.
Suspended SWCNTs (patterned Si)	1–1.3	250 V W^{-1}	40–60 ms	4.5×10^5	38
Suspended MWCNTs (patterned Si)	1–1.3	N/A	1–2 ms	3.3×10^6	39
Aligned SWCNTs (PVP matrix)	0.3–2	230 V W^{-1}	0.94 ms	1.2×10^8	40
Suspended MWCNTs (Ag antennas)	10.6	800 V W^{-1}	25 ms	1×10^7	41
Suspended aligned SWCNTs (polystyrene matrix)	2.5–20	500 V W^{-1}	150–200 ms	N/A	42
Suspended SWCNTs (PNIPAm matrix)	1–20	48 V W^{-1}	83 ms	N/A	43
DWCNT film (SiO_2/Si substrate)	1–1.3	5×10^4 V W^{-1}	1.5–2 ms	2×10^7	44
Suspended MWCNTs	0.94	110 V W^{-1}	750 ms	4×10^6	45
Suspended CNTs	0.375–118.8	50.9 mA W^{-1}	70 ms	3.5×10^7	24
Suspended Cs_xWO_3–CNTs	0.405–1.550	99.65 mA W^{-1}	28 ms	1.69×10^7	This work

the irradiated area increased to 34.4 °C from the dark state temperature of 32.8 °C. The temperature increment is thus 1.6 °C. However, for the Cs_xWO_3–CNT device, after irradiation for the same time duration, the temperature in the irradiated area increased to 38.3 °C from the dark state temperature of 32.9 °C. This temperature increment thus reached 5.4 °C. The figures show that there is basically no difference in temperature between the two devices in the dark state, but the surface temperature of the effective working region of the Cs_xWO_3–CNT device is approximately 4 °C higher than that of the CNT device under the same illumination conditions. In the Cs_xWO_3 crystal structure, the Cs^+ doping and the formation of oxygen vacancies can produce large numbers of free electrons, and these free electrons will undergo reciprocal motion and generate oscillations under the action of the applied electromagnetic field. When the oscillation frequency is close to the frequency of the electromagnetic field, the structure will resonate, and incident light with the resonance frequency will be absorbed and converted into vibrational energy. In addition, because of the injection of Cs^+, the carriers in Cs_xWO_3 are bound to the tungsten position and they polarize the surrounding lattice to form small polaritons, which absorb the infrared light when it jumps between the W^{5+} and W^{6+} positions. Under the combined action of the local surface plasmon resonance and the small polariton hopping, the Cs_xWO_3 nanoclusters produce strong infrared absorption. When coupled with excellent photothermal conversion efficiency of Cs_xWO_3, this leads to a significant temperature increase in the Cs_xWO_3–CNT composite film.

All the important parameters (*i.e.*, the responsivity, the response time, and D^*) of the Cs_xWO_3–CNT photodetector are summarized and are compared with the corresponding parameters of other representative reported photodetectors with a bolometric effect-based mechanism, as shown in Table 2. These results show that our suspended Cs_xWO_3–CNT photodetector provides a broad-spectrum response, high detectivity, and good performance, thus demonstrating its promise for use in high-efficiency photodetection applications.

4. Conclusions

In summary, we prepared two types of photodetector based on a CNT thin film and a Cs_xWO_3–CNT composite film. We then compared the photodetection performances of these two devices over a wide spectral range from the VIS region (405 nm) to the SWIR region (1550 nm). The results showed that the modification provided by the Cs_xWO_3 nanoclusters on the surface of the CNT film could enhance the light absorption of these films, particularly in the IR band (800–2000 nm). In the Cs_xWO_3–CNT device, the strong light absorption ability and efficient photothermal conversion property of Cs_xWO_3 complement the photoresponse based on the bolometric effect of the CNTs, thus significantly improving the device performance. When compared with the CNT devices, the Cs_xWO_3–CNT device shows average increases of 400% in responsivity and 549% in specific detectivity over the broad spectral range from the VIS region (405 nm) to the SWIR region (1550 nm), in which the detection performance at 808 nm (NIR) has shown the greatest improvement, with a 609% increase in specific detectivity. In addition, the response speed of the Cs_xWO_3–CNT device is improved by 30% when compared with the CNT device. These results show that CNTs modified with Cs_xWO_3 nanoclusters represent a promising composite material. Nanomaterials with significant photothermal effects can be used to improve the performances of photodetectors with a bolometric effect-based mechanism. This therefore provides a new route toward the development of uncooled high-performance broadband photodetectors. The finding has great significance in the development of optical nanomaterials, broadband photodetector technology and photothermal therapy.

Conflicts of interest

There are no conflicts to declare.

Acknowledgements

This work was supported by Beijing Municipal Natural Science Foundation (no. 4192024) and National Natural Science Foundation of China (51972188).

References

1 S. Imtiaz, M. Siddiq, A. Kausar, S. T. Muntha, J. Ambreen and I. Bibi, *Chin. J. Polym. Sci.*, 2018, **4**, 445–461.
2 Y. R. Poudel and W. Li, *Mater. Today Phys.*, 2018, **7**, 7–34.
3 J. W. G. Wilder, L. C. Venema, A. G. Rinzler, R. E. Smalley and C. Dekker, *Nature*, 1998, **391**, 59–62.
4 M. Kociak, A. Y. Kasumov, S. Guéron, B. Reulet and H. Bouchiat, *Phys. Rev. Lett.*, 2003, **329**, 1321–1322.
5 S. Berber, Y. K. Kwon and D. Tomanek, *Phys. Rev. Lett.*, 2000, **84**, 4613–4616.
6 A. Yu, P. Ramesh, X. Sun, E. Bekyarova, M. E. Itkis and R. C. Haddon, *Adv. Mater.*, 2008, **20**, 4740–4744.
7 J. Hone, M. Whitney, C. Piskoti and A. Zettl, *Phys. Rev. B: Condens. Matter Mater. Phys.*, 1999, **59**, 2514–2516.
8 M. S. Dresselhaus, G. Dreseelhaus and P. C. Eklund, *Science of Fullerenes and Carbon Nanotubes*, 1996.
9 N. Yao and V. Lordi, *J. Appl. Phys.*, 1998, **84**, 1939–1943.
10 B. G. Demczyk, Y. M. Wang, J. Cumings, M. Hetman, W. Han, A. Zettl and R. O. Ritchie, *Mater. Sci. Eng., A*, 2002, **334**, 173–178.
11 K. Mylvaganam and L. C. Zhang, *Carbon*, 2004, **42**, 2025–2032.
12 M. F. Yu, O. Lourie, M. J. Dyer, K. Moloni, T. F. Kelly and R. S. Ruoffl, *Science*, 2000, **287**, 637–640.
13 T. Pichler, M. Knupfer, M. S. Golden, J. Fink and R. E. Smalley, *Phys. Rev. Lett.*, 1998, **80**, 4729–4732.
14 M. E. Itkis, S. Niyogi, M. E. Meng, M. A. Hamon, H. Hu and R. C. Haddon, *Nano Lett.*, 2002, **2**, 155–159.
15 M. E. Itkis, F. Borondics, A. Yu and R. C. Haddon, *Science*, 2006, **312**, 413–416.
16 Q. Zhang, E. H. Hároz, Z. Jin, L. Ren, X. Wang, R. S. Arvidson, A. Lüttge and J. Kono, *Nano Lett.*, 2013, **13**, 5991–5996.

17 K. C. Chiu, A. L. Falk, P. H. Ho, D. B. Farmer and S. J. Han, *Nano Lett.*, 2017, **17**, 5641–5645.
18 A. Fujiwara, Y. Matsuoka, H. Suematsu, N. Ogawa and Y. Achiba, *Nanonetwork Materials*, 2001, vol. 590, pp. 35–44.
19 Y. Liu, F. Wang, X. Wang, X. Wang, E. Flahaut, X. Liu, Y. Li, X. Wang, Y. Xu, Y. Shi and R. Zhang, *Nat. Commun.*, 2015, **6**, 8589.
20 M. S. Arnold, J. D. Zimmerman, C. K. Renshaw, X. Xu and S. R. Forrest, *Nano Lett.*, 2009, **9**, 3354–3358.
21 X. He, N. Fujimura, J. M. Lloyd, K. J. Erickson, A. A. Talin, Q. Zhang, W. Gao, Q. Jiang, Y. Kawano and R. H. Hauge, *Nano Lett.*, 2014, **14**, 3953–3958.
22 S. Nanot, A. W. Cummings, C. L. Pint, A. Ikeuchi and J. Kono, *Sci. Rep.*, 2013, **3**, 1335.
23 M. Mahjouri-Samani, Y. S. Zhou, X. N. He, W. Xiong, P. Hilger and Y. F. Lu, *Nanotechnology*, 2012, **24**, 035502.
24 Y. Liu, J. Yin, P. Wang, Q. Hu, Y. Wang, Y. Xie, Z. Zhao, Z. Dong, J. L. Zhu and W. Chu, *ACS Appl. Mater. Interfaces*, 2018, **10**, 36304–36311.
25 O. Zivkovic, C. Yan and M. J. Wagner, *J. Mater. Chem.*, 2009, **19**, 6029–6033.
26 L. Chen, S. Lam, Q. Zeng, R. Amal and A. Yu, *J. Phys. Chem. C*, 2012, **116**, 11722–11727.
27 K. A. Willets and R. V. Duyne, *Annu. Rev. Phys. Chem.*, 2007, **58**, 267–297.
28 K. Adachi and T. Asahi, *J. Mater. Res.*, 2012, **27**, 965–970.
29 C. Guo, S. Yin, H. Yu, S. Liu, Q. Dong, T. Goto, Z. Zhang, Y. Li and T. Sato, *Nanoscale*, 2013, **5**, 6469–6478.
30 Z. Yu, Y. Yao, J. Yao, L. Zhang, Z. Chen, Y. Gao and H. Luo, *J. Mater. Chem. A*, 2017, **5**, 6019–6024.
31 A. A. Tessema, C. M. Wu, K. G. Motora and S. Naseem, *Compos. Sci. Technol.*, 2021, **211**, 108865.
32 C. Guo, S. Yin, M. Yan and T. Sato, *J. Mater. Chem.*, 2011, **21**, 5099–5105.
33 C. Guo, S. Yin, L. Huang and S. T. Yang, *Chem. Commun.*, 2011, **47**, 8853–8855.
34 Z. Li, Y. Jia, J. Wei, K. Wang, Q. Shu, X. Gui, H. Zhu, A. Cao and D. Wu, *J. Mater. Chem.*, 2010, **20**, 7236–7240.
35 S. M. Bachilo, M. S. Strano, C. Kittrell, R. H. Hauge, R. E. Smalley and R. B. Weisman, *Science*, 2002, **298**, 2361–2366.
36 S. Park, S. J. Kim, J. H. Nam, G. Pitner, T. H. Lee, A. L. Ayzner, H. L. Wang, S. W. Fong, M. Vosgueritchian, Y. J. Park, M. L. Brongersma and Z. N. Bao, *Adv. Mater.*, 2015, **27**, 759–765.
37 L. X. Benedict, S. G. Louie and M. L. Cohen, *Solid State Commun.*, 1996, **100**, 177–180.
38 R. Lu, Z. Li, G. Xu and J. Z. Wu, *Appl. Phys. Lett.*, 2009, **94**, 163110.
39 F. J. Baca, J. J. Shi, J. Z. Wu and R. Lu, *J. Appl. Phys.*, 2010, **108**, 084305.
40 G. Vera-Reveles, T. J. Simmons, M. Bravo-SaNchez, M. A. Vidal, H. Navarro-Contreras and F. J. GonzaLez, *ACS Appl. Mater. Interfaces*, 2011, **3**, 3200–3204.
41 M. Mahjouri-Samani, Y. S. Zhou, X. N. He, W. Xiong, P. Hilger and Y. F. Lu, *Nanotechnology*, 2012, **24**, 035502.
42 A. Y. Glamazda, V. A. Karachevtsev, W. B. Euler and I. A. Levitsky, *Adv. Funct. Mater.*, 2012, **22**, 2177–2186.
43 G. E. Fernandes, H. K. Jin, A. K. Sood and J. Xu, *Adv. Funct. Mater.*, 2013, **23**, 4678–4683.
44 C. Christianson, R. Lu and J. Wu, *Nanotechnology*, 2014, **25**, 425503.
45 J. John, M. Muthee, M. Yogeesh, S. K. Yngvesson and K. R. Carter, *Adv. Opt. Mater.*, 2014, **2**, 581–587.